ACS APPLIED NANO MATERIALS
Cite This: ACS Appl. Nano Mater. 2019, 2, 4095−4103
Article
www.acsanm.org

α-Ga_2O_3 Nanorod Array−Cu_2O Microsphere p−n Junctions for Self-Powered Spectrum-Distinguishable Photodetectors

Chenran He,[†] Daoyou Guo,[*,†,‡] Kai Chen,[†] Shunli Wang,[†] Jingqin Shen,[†] Nie Zhao,[§] Aiping Liu,[†] Yingying Zheng,[†] Peigang Li,[*,‡] Zhenping Wu,[‡] Chaorong Li,[†] Fengmin Wu,[†] and Weihua Tang[‡]

[†]Center for Optoelectronics Materials and Devices & Key Laboratory of Optical Field Manipulation of Zhejiang Province, Department of Physics, Zhejiang Sci-Tech University, Hangzhou 310018, China.

[‡]Laboratory of Information Functional Materials and Devices & State Key Laboratory of Information Photonics and Optical Communications, School of Science, Beijing University of Posts and Telecommunications, Beijing 100876, China

[§]College of Materials Science and Engineering, Xiangtan University, Xiangtan 411105, China

ABSTRACT: Most of the photodetectors can measure all of the light illumination with a wavelength below the absorption edge of the detector materials, while they cannot distinguish the different waveband. Herein, a self-powered spectrum-distinguishable photoelectrochemical (PEC) type photodetector based on an α-Ga_2O_3 nanorod array (NA)/Cu_2O microsphere (MS) p−n junction was reported. Under the combined action of the built-in electric field of the p−n junction and the semiconductor/electrolyte junction, the photodetector exhibits an opposite direction of the photocurrent to the illumination of 254 and 365 nm UV light under the applied bias of 0 V, which can be used to distinguish the different wavelengths of light. The photodetector shows a responsivity of 0.42 mA/W under 254 nm UV light and 0.57 mA/W upon 365 nm, respectively. Our results provide an idea for distinguishing the different illumination wavebands through a photodetector constructed by the heterojunction with two different band gap materials.

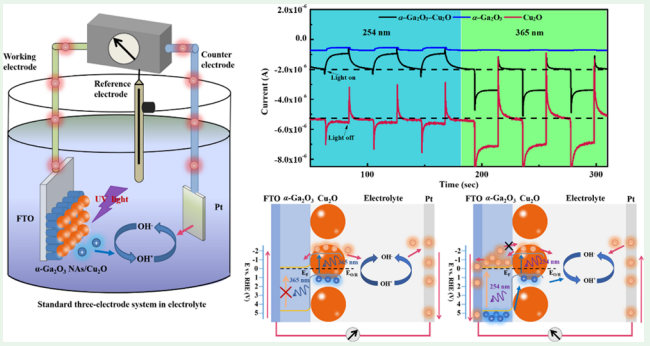

KEYWORDS: *p−n junction, Ga_2O_3/Cu_2O, solid/liquid junction, spectrum-distinguishable, self-powered*

INTRODUCTION

In the applications of environmental detection, implantable biological detector, and space detection, the demand for a high-performance photodetector is gradually increasing.[1−12] Conventional photodetectors cannot work independently and require additional power supply, which limits the convenience and applicability of them in various environments.[13−20] The self-powered photodetector based on photovoltaic effect can realize the conversion of light to electricity.[21−25] Thus, they can work by incident light instead of using batteries, which is more portable and environmentally friendly.[26−31] Photoconductive detectors are generally inferior to self-powered photodetectors in terms of response speed because of surface effects.[32] Considering the different interface properties of the heterojunction, the self-powered photodetectors can be divided into p−n junction type,[33,34] Schottky junction type,[35,36] photoelectrochemical (PEC) type,[37,38] etc. Because of the advantages of simple preparation process, low production cost, and good responsivity, the solid/liquid junction base PEC type photodetector composed of semiconductor and electrolyte has a good application prospect in varieties of harsh environments.[39,40]

Under the action of the interfacial space electric field of semiconductor/electrolyte, the PEC self-powered photodetector can effectively and rapidly separate photogenerated carriers and avoid their recombination.[41] Nowadays, most of the PEC type self-powered photodetectors that have been reported can measure all of the light with a wavelength below the absorption edge of the detector materials, while they cannot distinguish the wavelengths of different illumination.[42,43] Herein, we constructed a PEC type self-powered photodetector based on an n-type and a p-type semiconductor with different light absorption ranges for the application of spectrum-distinguishment. Varieties of metal oxide semiconductors including ZnO,[44] TiO_2,[45] SnO_2,[46] and Ga_2O_3[47−49] have been widely used in the field of photoelectric detection because of their suitable band gap and excellent photoelectric performance. α-Ga_2O_3, with a band gap of about 5.3 eV, is a direct band gap III−VI wide band gap semiconductor, which is a n-type semiconductor due to self-compensation effect.[50] Meanwhile, the vertical nanorod structure is conducive to the rapid

Received: March 20, 2019
Accepted: June 18, 2019
Published: June 18, 2019

DOI: 10.1021/acsanm.9b00527
ACS Appl. Nano Mater. 2019, 2, 4095−4103

transmission and separation of photogenerated carriers. The large specific surface area of nanorod arrays ensures a sufficient contact area between Ga_2O_3 and electrolyte solutions.

Cu_2O with a band gap of 2.0 eV is widely used in the field of photoelectric detection because of its simple and nontoxic synthesis method.[51] As we know, in the case of Cu vacancies and excess oxygen, Cu_2O is usually a *p*-type semiconductor.[52] When the *n*-type semiconductor α-Ga_2O_3 combined with Cu_2O, α-Ga_2O_3 NA/Cu_2O MS *p*−*n* junctions were obtained, which can effectively promote the separation of photoinduced carriers and broaden the range of light detection.[53] In addition, under the action of the *p*−*n* junction and solid/liquid junction, the spectrum-distinguishable feature of the detector can be realized.

In this work, we report a self-powered spectrum-distinguishable photodetector based on α-Ga_2O_3 NA/Cu_2O microsphere (MS) *p*−*n* junctions. α-Ga_2O_3 NAs were obtained by a hydrothermal method and post annealing treatment, and then α-Ga_2O_3 NAs/Cu_2O MS *p*−*n* junctions were constructed through a chemical bath deposition (CBD) process. The α-Ga_2O_3 NA/Cu_2O MS *p*−*n* junction photodetector shows a spectrum-distinguishable feature with an opposite photocurrent response upon the illumination of 254 and 365 nm ultraviolet light without bias, which is a promising candidate of distinguishable UV band self-powered photodetectors.

EXPERIMENTAL SECTION

Copper dinitrate [$Cu(NO_3)_2$], Tris(2-hydroxyethyl)Amine ($C_6H_{15}NO_3$, 98%), and Hydrazine hydrate ($N_2H_4{\cdot}H_2O$, 80%) were got from Shanghai Macklin Biochemical Co., Ltd. Gallium nitrate hydrate [$Ga(NO_3)_3{\cdot}xH_2O$, 99.99%] was obtained from Alfa Aesar Co., Ltd. The fluorine-doped tin oxide layer on the surface of the commercial FTO substrate (Shanghai Daheng Optics and Fine Mechanics Co., Ltd.) was used as the seed crystal layer for the growth of nanorods.

After hydrothermal reaction and post annealing treatment, the α-Ga_2O_3 NAs were obtained. The FTO glass was treated with acetone, anhydrous ethanol and deionized water in turn before use. A layer of SnO_2 on the surface of the FTO was used as a seed layer for the growth of GaOOH NAs. The $Ga(NO_3)_3$ with a concentration of 0.39 M/L was used as a precursor solution. Subsequently, the FTO glass was placed in the lining of the hydrothermal kettle containing the precursor solution. After heating at 150 °C for 12 h, the GaOOH NAs was obtained. Finally, the dried GaOOH NAs were annealed at 400 °C for 4 h to obtain α-Ga_2O_3 NAs.

The Cu_2O MSs was synthesized on the α-Ga_2O_3 NAs by chemical bath deposition (CBD). 0.05 M (0.4832g) $Cu(NO_3)_2$ and 1.5 M (10.194 mL) Tris(2-Hydroxyethyl)Amine were evenly distributed in a certain amount of DI water after stirring. Here the TEA was used as a complexing agent. Then keep the substrate with α-Ga_2O_3 NAs vertically in the solution by using electrode holder. The 0.1 M (242.54 μL) hydrazine hydrate ($N_2H_4{\cdot}H_2O$) that we added is as a reducing agent. After 2 h of growth, the α-Ga_2O_3 NA/Cu_2O MS *p*−*n* junctions were obtained.

The structure, composition and other basic characterization of the materials were analyzed by the field-emission scanning electron microscopy (FESEM, Hitachi S-4800) and Bruker D8 Advance X-ray diffractometer (XRD). The energy level distribution and optical band gap of the materials were tested by UV−vis spectrophotometer (Hitachi U-3900) and X-ray photoelectron spectroscopy (Thermo Scientific K-Alpha XPS).

The photoresponse performance of the spectrum-distinguishable photodetector was tested by electrochemical system (CHI660E). The effective working area of the α-Ga_2O_3 NA/Cu_2O MS based UV detector is about 1 cm^2. A 0.5 M aqueous solution of Na_2SO_4 was used as the electrolyte, and the counter electrode here is a Pt sheet. The intensities of the ultraviolet lamp (300 W xenon lamp, PLS SXE300) were gradually increased from 300 to 2500 $\mu W/cm^2$.

RESULTS AND DISCUSSION

The top-view of the Ga_2O_3 NAs is shown in Figure 1a, and Figure 1b represents the cross-sectional FESEM image of

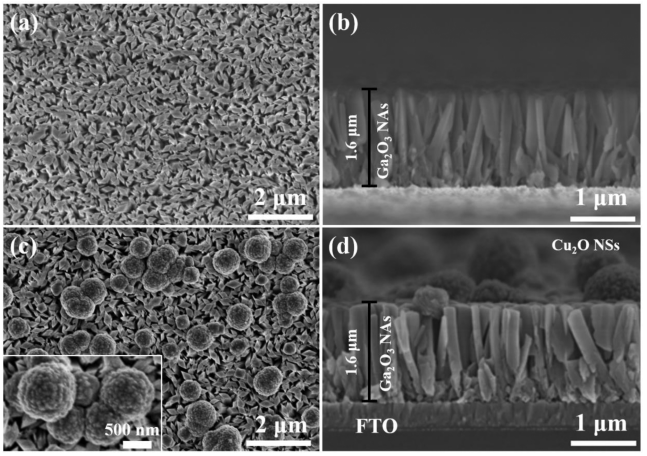

Figure 1. (a) Top-view FESEM image and (b) cross-sectional FESEM image of Ga_2O_3 NAs. (c) Top-view FESEM image and (d) cross-sectional FESEM image of Ga_2O_3 NAs/Cu_2O MSs, the inset is an enlarged view.

Ga_2O_3 NAs. It can be seen in Figure 1a that a uniform array of Ga_2O_3 nanorods grows vertically on FTO glass. The average diameter of the hexagonal-prism-like Ga_2O_3 nanorods ranges from 80 to 200 nm (Figure 1a) and a mean length of about 1.6 μm (Figure 1b). The Cu_2O MSs disperse on the Ga_2O_3 NAs after CBD process with an average diameter of about 1 μm, which can be seen in Figure 1c, d.

The XRD patterns of the FTO glass, Ga_2O_3 NAs and Ga_2O_3 NAs/Cu_2O MSs are represented in Figure 2a. The diffraction peak of FTO glass is due to the presence of the SnO_2 layer. In addition, the (110), (300) and (220) crystal planes of α phase Ga_2O_3 can be observed by the three diffraction peaks at 36.0, 64.7, and 76.4°. After the process of chemical bath method, the existence of Cu_2O MSs can be observed from the three added peaks situated at 29.5,36.4, and 42.2°, which can be indexed to (110), (111), and (200) planes of Cu_2O. Significant diffraction peaks of Cu and CuO were not observed, indicating that $Cu(NO_3)_2$ was completely reduced in the CBD process. And no additional diffraction peaks of possible impurities were detected.

To further study the chemical states of each element in α-Ga_2O_3 NAs/Cu_2O MSs, the XPS test was performed. As presented in Figure 2b that the peaks at 21.7, 397.3, 424.1, 1117.7, and 1144.8 eV could be attributed to Ga 3d, Ga LMM1, Ga LMM, and Ga 2p, respectively. Characteristic peaks of C 1s, Cu 2p, Cu 3p, Cu 3s, Cu 3d, Cu S, and Cu Auger are also observed in Figure 2b. Figure 2e shows the core energy level of Cu 2p, from which the oxidation state of Cu element in Cu_2O MSs can be further determined. In addition, the binding energies of Cu 2p 3/2 and Cu 2p 1/2 can also be determined by peaks located at 932.4 and 952.2 eV.[54]

Figure 2c presents the IR spectra of the α-Ga_2O_3 NAs, which has a *R*3*c* symmetrical corundum structure, and its crystal structure can be described by GaO_6 octahedron. Therefore, the broadband peak centered at 668 cm^{-1} can be interpreted as the

DOI: 10.1021/acsanm.9b00527
ACS Appl. Nano Mater. 2019, 2, 4095−4103

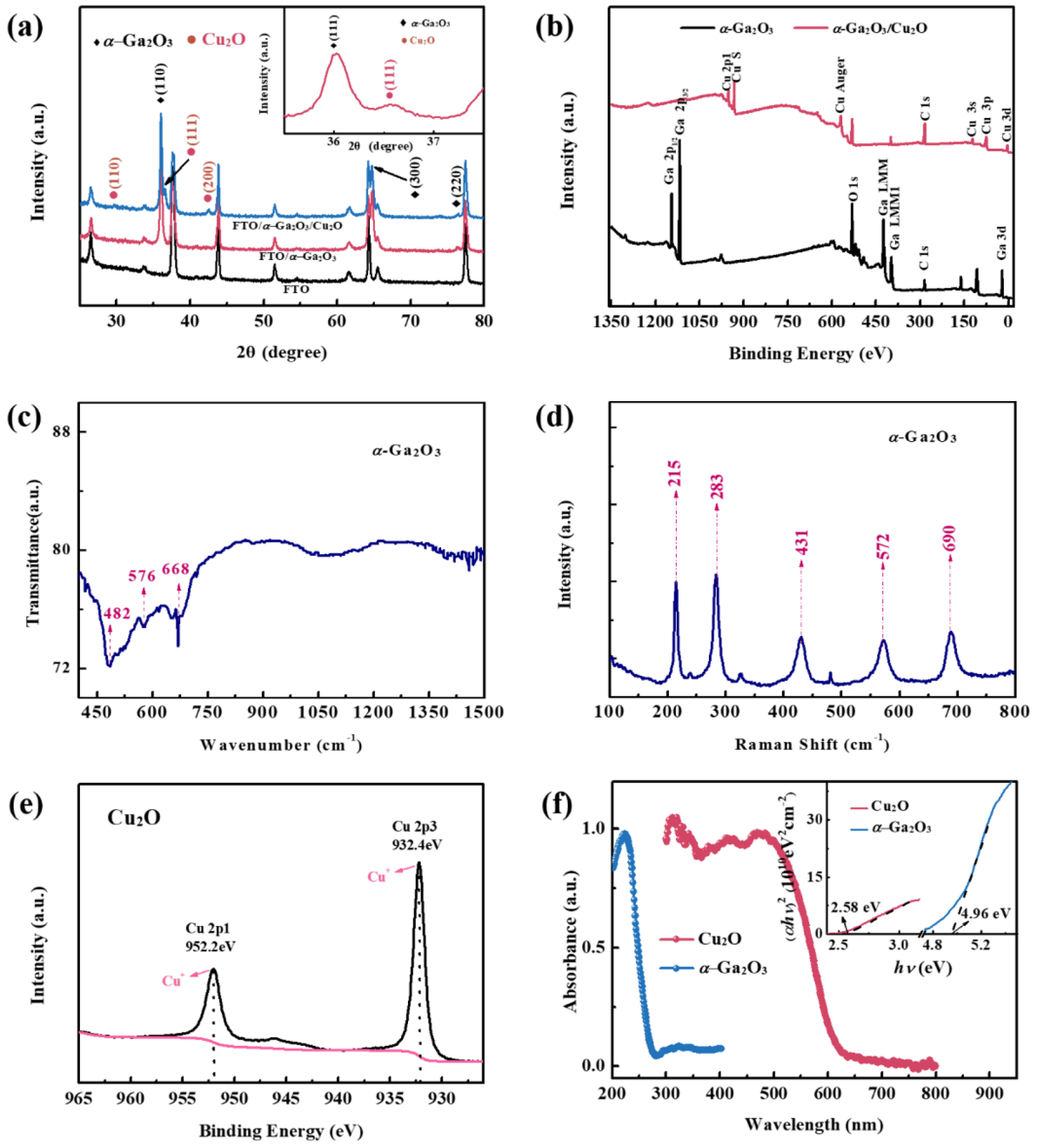

Figure 2. (a) XRD patterns of the FTO, FTO/Ga_2O_3 NAs, and FTO/Ga_2O_3 NAs/Cu_2O MSs. (b, e) the XPS spectra of Ga_2O_3 NAs/Cu_2O MSs. (c) Infrared spectrum and (d) Raman spectrum of α-Ga_2O_3 NAs. (f) UV−vis absorption spectra of the Ga_2O_3 and Cu_2O MSs, insert is the plot of $(\alpha h\nu)^2$ versus the energy of light ($h\nu$).

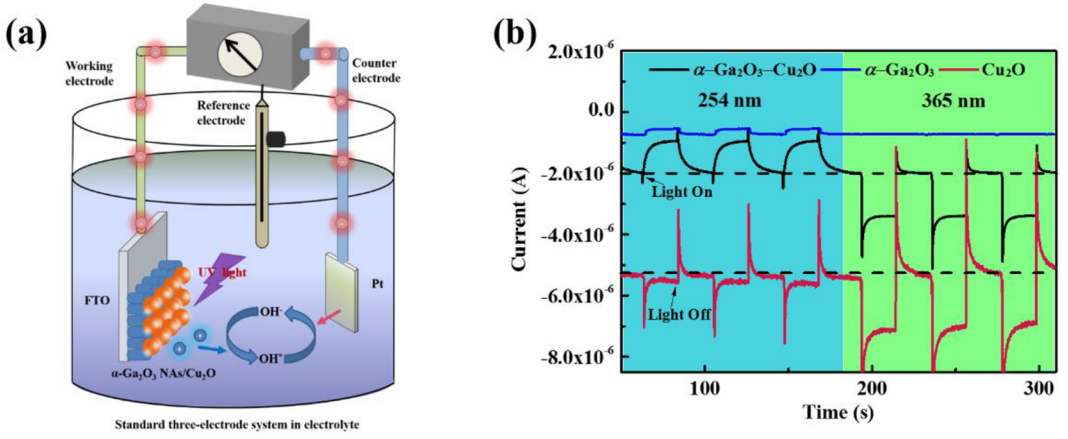

Figure 3. (a) Typical PEC system built for evaluating the photoresponse behaviors of the α-Ga_2O_3 NA/Cu_2O MS *p-n* junctions based photodetector. (b) Transient current upon 254 and 365 nm UV light on/off cycles for the photodetector at zero bias.

DOI: 10.1021/acsanm.9b00527
ACS Appl. Nano Mater. 2019, 2, 4095−4103

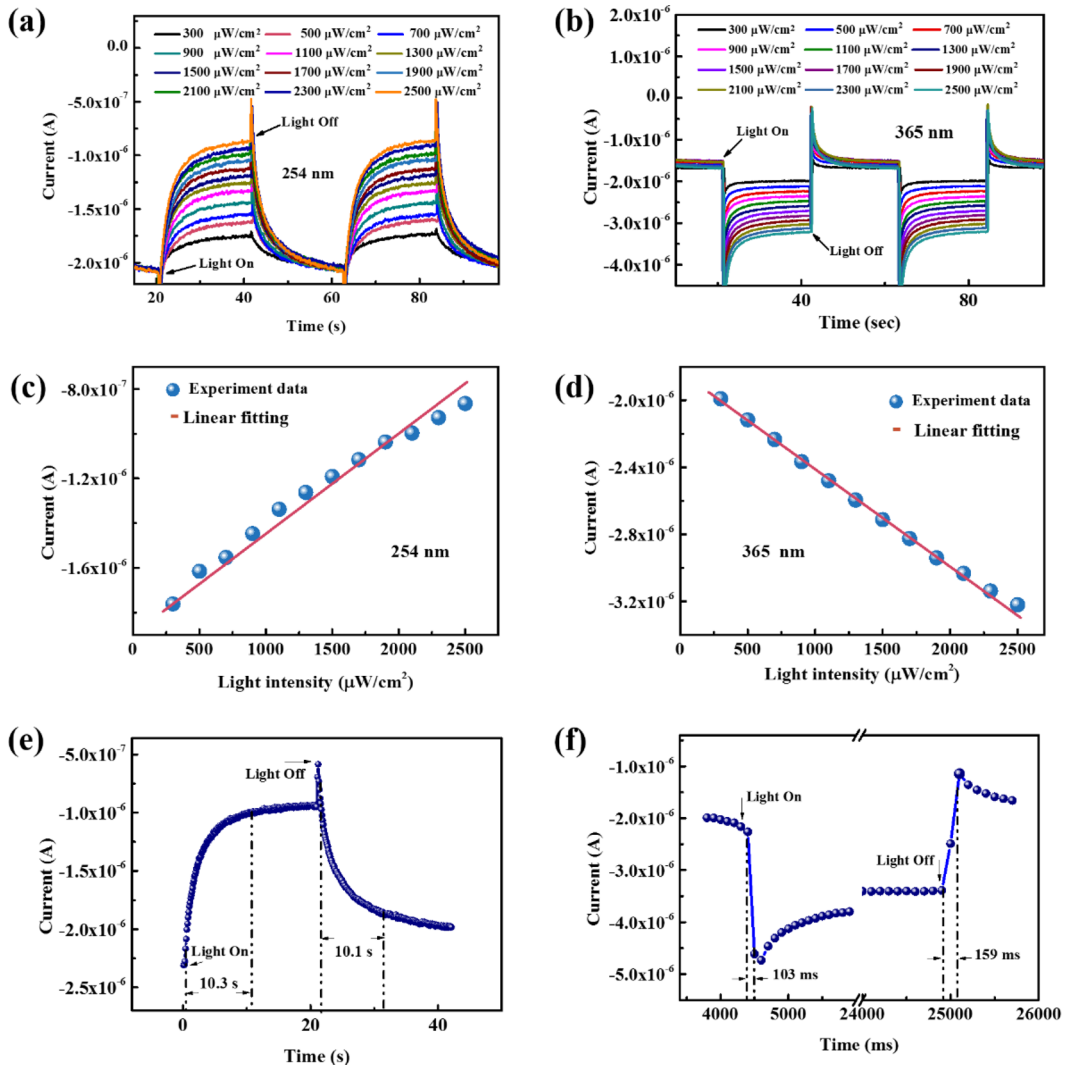

Figure 4. (a, b) Photoresponse of the device upon 254 and 365 nm UV light with various intensities. (c, d) Relationship between the light intensity and photocurrent. (e, f) Magnified rise and decay edges of the current response.

Ga−O vibration of the GaO_6 octahedral lattice in α-Ga_2O_3 NAs in the IR. In the Raman spectrum of α-Ga_2O_3 NAs (Figure 2d), the frequency peak range is related to different vibration modes. The high-frequency peak exceeding 600 cm^{-1} is derived from the symmetric stretching vibration of v1 of GaO_4; in the range of Raman shifts of 300 and 600 cm^{-1}, the peak corresponds to the symmetric stretching vibration of the GaO6 octahedron. The low-frequency peak below 200 cm^{-1} is caused by the O−Ga−O bending vibration of the GaO_6 octahedron. The Raman spectrum and IR of α-Ga_2O_3 NAs indicates the high crystal quality of α-Ga_2O_3 NAs, which is consistent with the XRD patterns.

The UV−visible absorbance spectra of α-Ga_2O_3 NAs and Cu_2O MSs are displayed in Figure 2f. To avoid interference from FTO glass, we tested the UV−vis absorbance of α-Ga_2O_3 by α-Ga_2O_3 nanorods powder loaded on a glass slide. It can be seen that the pure α-Ga_2O_3 is a good solar-blind photodetection material,[55] whereas the Cu_2O shows a broader light absorption range.[56] The optical band gaps of α-Ga_2O_3 NAs and Cu_2O MSs were calculated by using the equation $((\alpha h\nu)^2 = A(h\nu - E_g))$, which is shown in the inset of Figure 2f. The optical band gap of α-Ga_2O_3 NAs is estimated to be ∼4.96 eV and that of Cu_2O MSs is ∼2.58 eV. Consequently, strong visible light absorption of Cu_2O MSs expands the light detection range of α-Ga_2O_3 NAs and the remarkable light band distinguishing performance of such a structure is expected.

Figure 3a shows a standard three-electrode system based on an electrochemical system for testing the typical photoresponse characteristics of the detector. The α-Ga_2O_3 NA/Cu_2O MS $p-n$ junctions and platinum sheet were used as the working electrode and counter electrode, respectively. In addition, saturated calomel was used as the reference electrode to ensure the stability of the system. As a control, pure α-Ga_2O_3 NAs and Cu_2O MSs were also tested as working electrodes under the same conditions.

It can be seen in Figure 3b that the photoresponse performance of the detector under the illumination of different wavelengths and various intensities can be tested by switching on and off the UV lamp periodically. In dark, the α-Ga_2O_3 NA/Cu_2O MS $p-n$ junction exhibits a negative dark current of about −2.00 μA without bias voltage. A typical steady-state current of −0.90 μA was generated when the α-Ga_2O_3 NA/Cu_2O MS $p-n$ junction was upon 254 nm UV light. The ΔI ($I_{ph} - I_{dark}$) is calculated to be 1.10 μA. The detector shows a considerable stability after several cycles.[57,58] It is noteworthy that when the illumination switches to 365 nm ultraviolet light,

DOI: 10.1021/acsanm.9b00527
ACS Appl. Nano Mater. 2019, 2, 4095−4103

Table 1. Comparison of the Key Parameters of the α-Ga_2O_3 NA/Cu_2O MS $p-n$ Junction Self-Powered Photodetectors and Other Previously Reported Devices

materials	device type	illumination (nm)	responsivity (μA/W)	response time	ref.
2D Bi_2S_3	PEC	300−800	8.9 (365 nm)	0.1/0.1 s (400 nm)	38
Te nanosheet	PEC	350−475	1.85−2.15		43
$BiQD_s$	PEC	200−600	19.3(350 nm)	0.1/0.2 s (350 nm)	53
ZnO/SnS	heterojunction	365	3.64×10^5	49.1/51.8 s	57
ZnO/SnS	heterojunction	690	1.55×10^5	0.4/0.2 s	57
α-Ga_2O_3/Cu_2O	PEC	254	4.2×10^2	10.3/10.1 s	this work
α-Ga_2O_3/Cu_2O	PEC	365	5.7×10^2	103/159 ms	this work

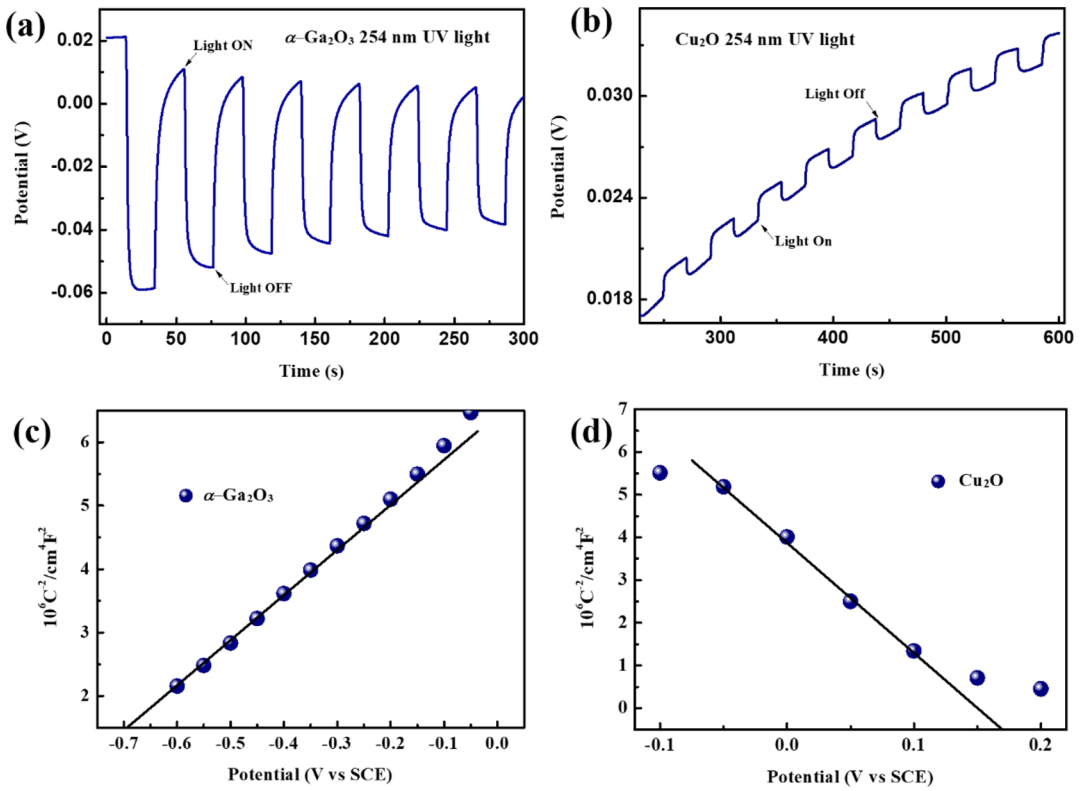

Figure 5. Open circuit potential transient upon chopping illumination of pure (a) α-Ga_2O_3 NAs, (b) Cu_2O MSs; Mott−Schottky plots of pure (c) α-Ga_2O_3 NAs and (d) Cu_2O MSs measured in an aqueous solution of Na_2SO_4 (0.5 M).

the α-Ga_2O_3 NA/Cu_2O MS $p-n$ junction exhibits an opposite direction of photoresponse current with a value of −3.40 μA. And the ΔI ($I_{ph} - I_{dark}$) is −1.40 μA. It means that this detector can distinguish the 254 and 365 nm ultraviolet light according to the positive and negative values of ΔI ($I_{ph} - I_{dark}$). For the purpose of comparison, photoresponse properties of pure α-Ga_2O_3 NAs and Cu_2O MSs were also studied under the same irradiation conditions. As a comparison, Figure 3b shows the photocurrent of pure α-Ga_2O_3 NAs and pure Cu_2O MSs. The initial dark current of pristine α-Ga_2O_3 NAs was −0.73 μA and the photocurrent was only −0.54 μA. Moreover, the pure α-Ga_2O_3 NAs almost has no response to 365 nm ultraviolet light. As for pure Cu_2O MSs, they exhibit a preferable performance exposure to 365 nm ultraviolet light versus 254 nm ultraviolet light. In contrast to the pure α-Ga_2O_3 NAs and Cu_2O MSs, the α-Ga_2O_3 NA/Cu_2O MS $p-n$ junction exhibits a better responsivity and a light−dark current ratio.

The $I-t$ curves of α-Ga_2O_3 NA/Cu_2O MS $p-n$ junction under different intensities of 254 and 365 nm UV irradiation are shown in Figure 4a, b. The photocurrent was enhanced with the increase of light intensity. Furthermore, as presented in Figure 4c, d, the photocurrent of α-Ga_2O_3 NA/Cu_2O MS $p-n$ junction exhibits an obvious light intensity-dependent character with the increase of light intensity from 300 to 2500 $\mu W/cm^2$.

Photoresponsivity is an important reference to assess the performance of a detector. The photocurrent generated by the unit effective area of the detector under a certain power of illumination is defined as R_λ, which can be calculated by this equation:[59]

$$\Delta I = I_{ph} - I_{dark} \quad (1)$$

$$R_\lambda = \Delta I/(PS) \quad (2)$$

where ΔI is the change of current in the detector after illumination. P is the power density of ultraviolet lamp and S is the effective illumination area of the α-Ga_2O_3 NA/Cu_2O MS $p-n$ junctions on FTO. When the power density of the UV lamp is 2500 $\mu W/cm^2$, the R of α-Ga_2O_3 NA/Cu_2O MS $p-n$ junction upon 254 nm UV light is 0.42 mA/W. And that is 0.57 mA/W for 365 nm UV light.

DOI: 10.1021/acsanm.9b00527
ACS Appl. Nano Mater. 2019, 2, 4095−4103

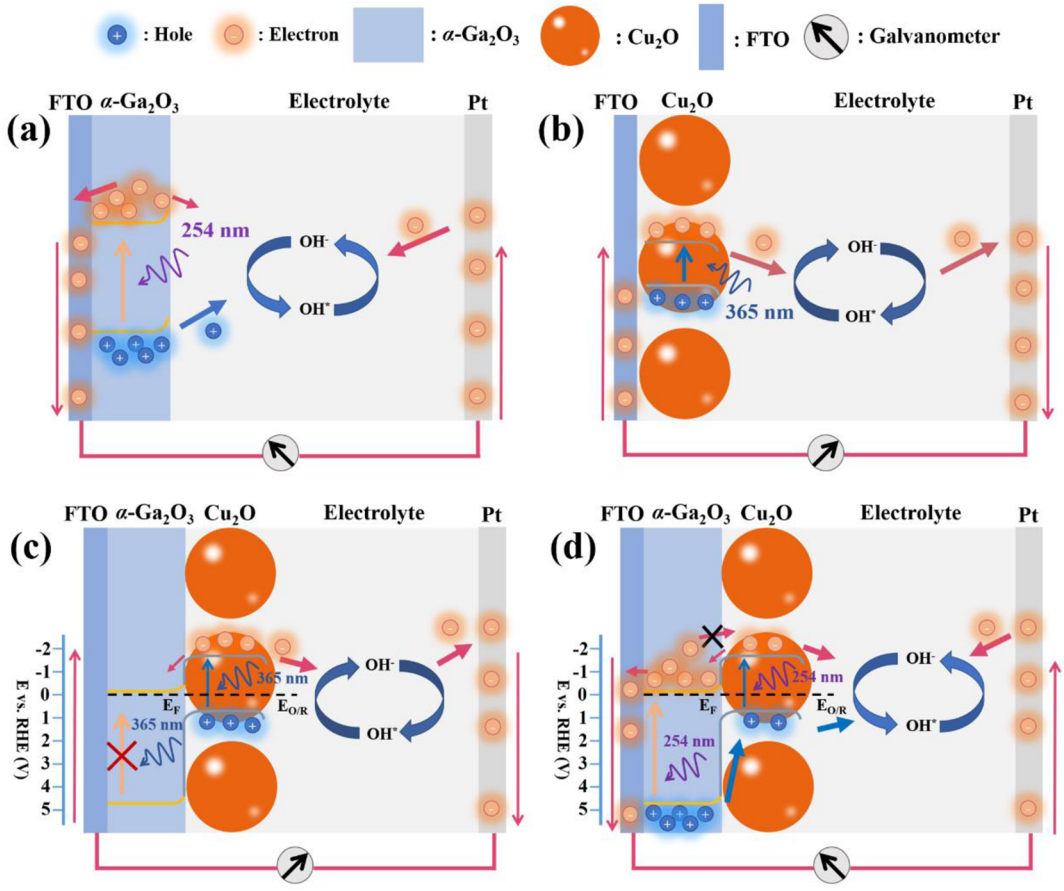

Figure 6. Schematic diagram of the self-powered α-Ga_2O_3 NA/Cu_2O MS p−n junction photodetectors.

The photoresponse time of the detector are respectively defined as the time required for the current to increase from 10 to 90% of the peak value, and vice versa.[56] As shown in Figure 4e, f, the rise time and decay time of α-Ga_2O_3 NA/Cu_2O MS p−n junction upon 254 nm UV light are about 10.3 and 10.1 s, respectively. And upon to 365 nm UV light these are 103 and 159 ms, exhibit the fast response speed. Besides α-Ga_2O_3 NA/Cu_2O MS p−n junction, some emerging new materials had been developed for novel photodetector. Such as few-layer BP nanosheets,[40] 2D InSe nanosheets,[39] 2D nonlayered Te nanosheets, ZnO NWs/shuttle-like SnS[59] and MoS_2/graphene.[37] Table 1 compares the photoelectric performance of self-powered α-Ga_2O_3/Cu_2O p−n junction photodetector with the researches of others. Compared with the previous reports, our photodetector based on α-Ga_2O_3/Cu_2O p−n junction has good responsivity and the fastest response speed upon 365 nm UV light.

Figure 5a, b show the open circuit potential (OCP) curves of pure α-Ga_2O_3 NAs and Cu_2O MSs upon chopped illumination of 254 nm ultraviolet light. The negative change of open-circuit potential upon illumination proves the upward energy band bending in the interfacial built-in electric field of α-Ga_2O_3 NAs/electrolyte (0.5 M Na_2SO_4). Thus, the α-Ga_2O_3 NAs is an n-type semiconductor.[60] Conversely, the positive OCP transient in Figure 5b indicates that the Cu_2O MSs is an p-type semiconductor. Obviously, the α-Ga_2O_3/Cu_2O heterojunction space charge region is formed after p-type Cu_2O MSs loaded on the n-type α-Ga_2O_3 NAs. Mott−Schottky (MS) measurements were carried out to further verify the conduction type of the semiconductors and determine the band structure. As shown in Figure 5c, d, the opposite directions of the slopes indicate the different conductivity types of α-Ga_2O_3 and Cu_2O. The flat potential E_{fb} at the interface between semiconductor and solution can be calculated using the Mott−Schottky relation:[61]

$$1/C^2 = (2/e\varepsilon\varepsilon_0 N)[(E - E_{fb}) - kT/e] \quad (3)$$

Where C is the capacitance of the semiconductor electrode per unit area, E_{fb} is the flat band potential, E is the electrode potential, ε is the relative dielectric constant of the semiconductor (here the ε of α-Ga_2O_3 is 10 and that of Cu_2O is 7.6),[62,63] ε_0 is the vacuum dielectric constant, k is the Boltzmann constant, and T is the absolute temperature. e is the basic charge, at room temperature, and kT/e is about 0.026 V, which is negligible.

In the $1/C^2$-E diagram, the straight-line extension of $1/C^2$ intersects the potential E axis at E_{fb}. Thus, the flat band potential of the semiconductor electrode was obtained. As shown in Figure 5c, d, the E_{fb} of the α-Ga_2O_3 NAs is −0.70 V (vs SCE) and that of Cu_2O MSs locates at 0.17 (vs SCE). The E_{fb} is usually switched to the normal hydrogen electrode (NHE) scale using the Nernst equation for subsequent calculations.[64]

$$E_{NHE} = E\ (\text{vs SCE}) + 0.0591pH + 0.244 \quad (4)$$

The E_{fb} of the α-Ga_2O_3 NAs locates at −0.0423 V (RHE) and that of Cu_2O MSs locates at 0.8277 (RHE). According to the change of semiconductor Fermi energy level before and after contact with solution, the energy band bending of solid/liquid

DOI: 10.1021/acsanm.9b00527
ACS Appl. Nano Mater. 2019, 2, 4095−4103

junction space electric field can be calculated by using equation: $V_{sc} = E_{OCP} - E_{fb}$.[60] The band bending across the solid/liquid junction of α-Ga_2O_3 NAs is calculated to be 0.72 V and that of Cu_2O MSs is −0.12 V. It can be considered that the flat band potential E_{fb} is approximately the bottom of the conduction band for *n*-type semiconductor, or the top of the valence band for the *p*-type semiconductor.[60] Combined with the optical band gap of α-Ga_2O_3 (4.96 eV) and Cu_2O (2.58 eV) we have measured, the electronic energy band diagram of the heterojunction can be given easily.

Figure 6 shows the mechanism of spectrum-distinguishable photodetector based on α-Ga_2O_3 NA/Cu_2O MS *p*−*n* junction operated without bias. When the semiconductor (solid) in contact with the electrolyte (liquid), the condition for the semiconductor/solution system to reach an equilibrium is that the Fermi level (E_f) of the semiconductor at the interface equal to the Redox couple level ($E_{O/R}$) of the solution.[65] The band structure diagram of α-Ga_2O_3 NA/Cu_2O MS *p*−*n* junction under the scale of normal hydrogen electrode (NHE) is shown in Figure 6, and the band positions of α-Ga_2O_3 and Cu_2O were given. As shown in Figure 6a, because of the influence of the redox couple in the solution, the carrier distribution of the pure α-Ga_2O_3 NAs changed, forming a space charge region and an upward energy band bending. Photoinduced electrons excited in pure α-Ga_2O_3 would transfer to FTO driven by the space-charge region of α-Ga_2O_3/electrolyte junction under 254 nm UV light. Several photoinduced electrons also diffuse to the electrolyte because of the large specific surface area of nanorods.[66] In the meantime, photon-induced holes also transport into the electrolyte and trap the electrons of OH^- ($h^+ + OH^- = OH^*$) at the solid/liquid interface. The positive OH* was then reduced at the counter electrode ($e^- + OH^* = OH^-$) to form a current loop. In addition, no significant photocurrent was observed upon 365 nm ultraviolet light due to the large band gap of pure α-Ga_2O_3. Conversely, the direction of built-in electric field at Cu_2O/electrolyte interface is opposite to that of α-Ga_2O_3/electrolyte due to the different types of conduction. Under the illumination of 254 or 365 nm ultraviolet light, photoinduced electrons in the conduction band of the pure Cu_2O transfer to electrolyte and then oxidized at the counter electrode, which forms the photocurrent in opposite direction compared with pure α-Ga_2O_3 NAs. Different photogenerated electrons transport directions upon to illumination in pure α-Ga_2O_3 NAs and Cu_2O MSs lead to different photoresponse currents, which corresponds to the result in Figure 3b.

As for the α-Ga_2O_3 NA/Cu_2O MS *p*-*n* junction upon to 254 nm UV light (Figure 3b), the device exhibits enhanced photoresponsivity than the pure α-Ga_2O_3 NAs. It can be attributed to two factors as follows (Figure 6d): (1) The as-formed built-in electric field in α-Ga_2O_3/Cu_2O heterojunction junctions effectively block the diffusion of the photoinduced electrons from α-Ga_2O_3 to the electrolyte; (2) a number of carriers would be generated in Cu_2O MSs, and then the photoinduced electrons would migrate from Cu_2O toward to α-Ga_2O_3 driven by the α-Ga_2O_3/Cu_2O *p*−*n* junctions. As a result, it would collect more electrons at the FTO, and produce an enhanced photocurrent. However, when the illumination turns to 365 nm UV light, the photoinduced carriers only can be produced in the Cu_2O MSs because of the only deep UV absorption of α-Ga_2O_3 NAs (Figure 6c). Noteworthily, the surface of Cu_2O MSs is completely immersed in electrolyte except the bottom, leading to a larger area of Cu_2O/electrolyte junction than α-Ga_2O_3/Cu_2O *p*−*n* junction. Therefore, although the photogenerated electrons in Cu_2O MSs can transport to both α-Ga_2O_3 NAs and electrolyte, most of the photogenerated electrons will transfer to the electrolyte. As a result, it shows the same directions of photocurrent as pure Cu_2O MSs (Figure 3b). These factors contribute to the difference in the photocurrent of the α-Ga_2O_3 NA/Cu_2O MS *p*−*n* junction upon 254 and 365 nm ultraviolet light. Thus, it can be seen, under the interaction of the space charge region of the α-Ga_2O_3 NA/Cu_2O MS *p*−*n* junction and the semiconductor/electrolyte junction, that the photodetector based on α-Ga_2O_3 NA/Cu_2O MS *p*−*n* junction exhibits a reverse photocurrent upon 254 and 365 nm UV light without bias. It provides an idea for distinguishing the different illumination wavebands by a photodetector constructed by the heterojunction with two different band gap materials.

CONCLUSIONS

In a word, a self-powered spectrum-distinguishable detector based on α-Ga_2O_3 NA/Cu_2O MS *p*−*n* junctions has been constructed successfully. Under the irradiation of 254 and 365 nm UV light, the different photoinduced electrons transport directions in the device lead to different photoresponse currents, which can be used to distinguish the wavelengths of these two kinds of illumination. α-Ga_2O_3 NA/Cu_2O MS *p*−*n* junction photodetector have a responsivity of 0.57 mA/W (0.42 mA/W) upon exposure to 365 (254) nm ultraviolet light. The detector also has a fast-operated speed with a rise time of 103 ms upon exposure to 365 nm ultraviolet light. The α-Ga_2O_3 NA/Cu_2O MS *p*−*n* junction-based PEC type self-powered photodetector we constructed is an interesting candidate for the application of spectrum-distinguishment.

AUTHOR INFORMATION

Corresponding Authors

*Email: dyguo@zstu.edu.cn (D.G.).
*Email: pgli@bupt.edu.cn (P.L.).

ORCID

Daoyou Guo: 0000-0002-6191-1655
Nie Zhao: 0000-0002-3824-9974
Aiping Liu: 0000-0002-2338-062X

Notes

The authors declare no competing financial interest.

ACKNOWLEDGMENTS

This work was supported by the National Natural Science Foundation of China (61704153, 51572241, 61774019, 51572033, 11605149), Zhejiang Public Service Technology Research Program/Analytical Test (LGC19F040001), Beijing Municipal Commission of Science and Technology (SX2018-04), and the Open Fund of IPOC (BUPT).

REFERENCES

(1) Guo, Y.; Li, Y.; Zhang, Q.; Wang, H. Self-powered multifunctional UV and IR photodetector as an artificial electronic eye. *J. Mater. Chem. C* **2017**, *5* (6), 1436−1442.

(2) Dong, L.; Yu, J.; Zhang, Y.; Jia, R. Elements (Si, Sn, and Mg) doped α-Ga_2O_3: First-principles investigations and predictions. *Comput. Mater. Sci.* **2019**, *156*, 273−279.

(3) Liu, Y.; Zhou, J.; Chen, L.; Zhang, P.; Fu, W.; Zhao, H.; Ma, Y.; Pan, X.; Zhang, Z.; Han, W.; Xie, E. Highly Flexible Freestanding Porous Carbon Nanofibers for Electrodes Materials of High-

DOI: 10.1021/acsanm.9b00527
ACS Appl. Nano Mater. 2019, 2, 4095−4103

Performance All-Carbon Supercapacitors. *ACS Appl. Mater. Interfaces* **2015**, *7* (42), 23515−20.
(4) Wang, X.; Cui, Y.; Li, T.; Lei, M.; Li, J.; Wei, Z. Recent Advances in the Functional 2D Photonic and Optoelectronic Devices. *Adv. Opt. Mater.* **2019**, *7*, 1801274.
(5) Cheng, G.; Zhou, P.; Han, J. Learning Rotation-Invariant Convolutional Neural Networks for Object Detection in VHR Optical Remote Sensing Images. *IEEE. Geosci. Remote. S.* **2016**, *54* (12), 7405−7415.
(6) Dong, L.; Jia, R.; Li, C.; Xin, B.; Zhang, Y. Ab initio study of N-doped β-Ga_2O_3 with intrinsic defects: the structural, electronic and optical properties. *J. Alloys Compd.* **2017**, *712*, 379−385.
(7) Zhang, P.; Zhou, J.; Chen, W.; Zhao, Y.; Mu, X.; Zhang, Z.; Pan, X.; Xie, E. Constructing highly-efficient electron transport channels in the 3D electrode materials for high-rate supercapacitors: The case of $NiCo_2O_4$@$NiMoO_4$ hierarchical nanostructures. *Chem. Eng. J.* **2017**, *307*, 687−695.
(8) Han, J.; Zhang, D.; Cheng, G.; Guo, L.; Ren, J. Object Detection in Optical Remote Sensing Images Based on Weakly Supervised Learning and High-Level Feature Learning. *IEEE. T. GEOSCI. REMOTE* **2015**, *53* (6), 3325−3337.
(9) Yang, Y.; Pradel, K. C.; Jing, Q.; Wu, J. M.; Zhang, F.; Zhou, Y.; Zhang, Y.; Wang, Z. L. Thermoelectric nanogenerators based on single Sb-doped ZnO micro/nanobelts. *ACS Nano* **2012**, *6* (8), 6984−6989.
(10) Luan, S.; Dong, L.; Jia, R. Analysis of the structural, anisotropic elastic and electronic properties of β-Ga_2O_3 with various pressures. *J. Cryst. Growth* **2019**, *505*, 74−81.
(11) Zhang, H.; Yang, Y.; Su, Y.; Chen, J.; Hu, C.; Wu, Z.; Liu, Y.; Ping Wong, C.; Bando, Y.; Wang, Z. L. Triboelectric nanogenerator as self-powered active sensors for detecting liquid/gaseous water/ethanol. *Nano Energy* **2013**, *2* (5), 693−701.
(12) Lin, Z. H.; Cheng, G.; Yang, Y.; Zhou, Y. S.; Lee, S.; Wang, Z. L. Triboelectric nanogenerator as an active UV photodetector. *Adv. Funct. Mater.* **2014**, *24* (19), 2810−2816.
(13) Zhang, H.; Jia, R.; Lei, Y.; Tang, X.; Zhang, Y.; Zhang, Y. Leakage current conduction mechanisms and electrical properties of atomic-layer-deposited HfO_2/Ga_2O_3 MOS capacitors. *J. Phys. D: Appl. Phys.* **2018**, *51* (7), 075104.
(14) Zhang, D.; Zheng, W.; Lin, R. C.; Li, T. T.; Zhang, Z. J.; Huang, F. High quality β-Ga_2O_3 film grown with N_2O for high sensitivity solar-blind-ultraviolet photodetector with fast response speed. *J. Alloys Compd.* **2018**, *735*, 150−154.
(15) Zhang, H.; Xiang, L.; Yang, Y.; Xiao, M.; Han, J.; Ding, L.; Zhang, Z.; Hu, Y.; Peng, L. M. High-Performance Carbon Nanotube Complementary Electronics and Integrated Sensor Systems on Ultrathin Plastic Foil. *ACS Nano* **2018**, *12* (3), 2773−2779.
(16) Zheng, W.; Lin, R.; Zhang, D.; Jia, L.; Ji, X.; Huang, F. Vacuum-Ultraviolet Photovoltaic Detector with Improved Response Speed and Responsivity via Heating Annihilation Trap State Mechanism. *Adv. Opt. Mater.* **2018**, *6* (21), 1800697.
(17) Bi, K.; Wang, X.; Hao, Y.; Lei, M.; Dong, G.; Zhou, J. Wideband slot-coupled dielectric resonator-based filter. *J. Alloys Compd.* **2019**, *785*, 1264−1269.
(18) Ma, Y.; Chen, W.; Zhang, P.; Teng, F.; Zhou, J.; Pan, X.; Xie, E. Ni(OH)2 nanosheets grown on a 3D graphene framework as an excellent cathode for flexible supercapacitors. *RSC Adv.* **2014**, *4* (88), 47609−47614.
(19) Bi, K.; Wang, X.; Hao, Y.; Lei, M.; Dong, G.; Zhou, J. Wideband slot-coupled dielectric resonator-based filter. *J. Alloys Compd.* **2019**, *785*, 1264−1269.
(20) He, X.; Luan, S. Z.; Wang, L.; Wang, R. Y.; Du, P.; Xu, Y. Y.; Yang, H. J.; Wang, Y. G.; Huang, K.; Lei, M. Facile loading mesoporous Co_3O_4 on nitrogen doped carbon matrix as an enhanced oxygen electrode catalyst. *Mater. Lett.* **2019**, *244*, 78−82.
(21) Quhe, R.; Liu, J.; Wu, J.; Yang, J.; Wang, Y.; Li, Q.; Li, T.; Guo, Y.; Yang, J.; Peng, H.; Lei, M.; Lu, J. High-performance sub-10 nm monolayer Bi_2O_2Se transistors. *Nanoscale* **2019**, *11* (2), 532−540.
(22) Zheng, W.; Lin, R.; Zhu, Y.; Zhang, Z.; Ji, X.; Huang, F. Vacuum Ultraviolet Photodetection in Two-Dimensional Oxides. *ACS Appl. Mater. Interfaces* **2018**, *10* (24), 20696−20702.
(23) Lin, Z.-H.; Cheng, G.; Yang, Y.; Zhou, Y. S.; Lee, S.; Wang, Z. L. Triboelectric Nanogenerator as an Active UV Photodetector. *Adv. Funct. Mater.* **2014**, *24* (19), 2810−2816.
(24) Guo, D.; Su, Y.; Shi, H.; Li, P.; Zhao, N.; Ye, J.; Wang, S.; Liu, A.; Chen, Z.; Li, C.; Tang, W. Self-Powered Ultraviolet Photodetector with Superhigh Photoresponsivity (3.05 A/W) Based on the GaN/Sn:Ga_2O_3 *pn* Junction. *ACS Nano* **2018**, *12* (12), 12827−12835.
(25) Li, S.; Wang, T.; Chen, X.; Lu, W.; Xie, Y.; Hu, Y. Self-powered photogalvanic phosphorene photodetectors with high polarization sensitivity and suppressed dark current. *Nanoscale* **2018**, *10* (16), 7694−7701.
(26) Yang, H.; Geng, L.; Zhang, Y.; Chang, G.; Zhang, Z.; Liu, X.; Lei, M.; He, Y. Graphene-templated synthesis of palladium nanoplates as novel electrocatalyst for direct methanol fuel cell. *Appl. Surf. Sci.* **2019**, *466*, 385−392.
(27) Zhong, W.; Tu, W.; Feng, S.; Xu, A. Photocatalytic H_2 evolution on CdS nanoparticles by loading FeSe nanorods as co-catalyst under visible light irradiation. *J. Alloys Compd.* **2019**, *772*, 669−674.
(28) Zhong, W.; Shen, S.; Feng, S.; Lin, Z.; Wang, Z.; Fang, B. Facile fabrication of alveolate Cu_2-xSe microsheets as a new visible-light photocatalyst for discoloration of Rhodamine B. *CrystEngComm* **2018**, *20* (48), 7851−7856.
(29) Lin, S.; Bai, X.; Wang, H.; Wang, H.; Song, J.; Huang, K.; Wang, C.; Wang, N.; Li, B.; Lei, M.; Wu, H. Roll-to-Roll Production of Transparent Silver-Nanofiber-Network Electrodes for Flexible Electrochromic Smart Windows. *Adv. Mater.* **2017**, *29* (41), DOI: 10.1002/adma.201770300
(30) Wang, H.; Liu, R.; Li, Y.; Lü, X.; Wang, Q.; Zhao, S.; Yuan, K.; Cui, Z.; Li, X.; Xin, S.; Zhang, R.; Lei, M.; Lin, Z. Durable and Efficient Hollow Porous Oxide Spinel Microspheres for Oxygen Reduction. *Joule* **2018**, *2* (2), 337−348.
(31) Wang, X.; Cui, Y.; Li, T.; Lei, M.; Li, J.; Wei, Z. Recent Advances in the Functional 2D Photonic and Optoelectronic Devices. *Adv. Opt. Mater.* **2019**, *7*, 1801274.
(32) Wang, H.; Liu, R.; Li, Y.; Lü, X.; Wang, Q.; Zhao, S.; Yuan, K.; Cui, Z.; Li, X.; Xin, S.; Zhang, R.; Lei, M.; Lin, Z. Durable and Efficient Hollow Porous Oxide Spinel Microspheres for Oxygen Reduction. *Joule* **2018**, *2* (2), 337−348.
(33) Li, P.; Shi, H.; Chen, K.; Guo, D.; Cui, W.; Zhi, Y.; Wang, S.; Wu, Z.; Chen, Z.; Tang, W. Construction of GaN/Ga_2O_3 *p-n* junction for an extremely high responsivity self-powered UV photodetector. *J. Mater. Chem. C* **2017**, *5* (40), 10562−10570.
(34) Zheng, L.; Teng, F.; Zhang, Z.; Zhao, B.; Fang, X. Large scale, highly efficient and self-powered UV photodetectors enabled by all-solid-state *n*-TiO_2 nanowell/*p*-NiO mesoporous nanosheet heterojunctions. *J. Mater. Chem. C* **2016**, *4* (42), 10032−10039.
(35) Gao, Z.; Jin, W.; Zhou, Y.; Dai, Y.; Yu, B.; Liu, C.; Xu, W.; Li, Y.; Peng, H.; Liu, Z.; Dai, L. Self-powered flexible and transparent photovoltaic detectors based on CdSe nanobelt/graphene Schottky junctions. *Nanoscale* **2013**, *5* (12), 5576−81.
(36) Wu, C.-Y.; Pan, Z.-Q.; Wang, Y.-Y.; Ge, C.-W.; Yu, Y.-Q.; Xu, J.-Y.; Wang, L.; Luo, L.-B. Core-shell silicon nanowire array-Cu nanofilm Schottky junction for a sensitive self-powered near-infrared photodetector. *J. Mater. Chem. C* **2016**, *4* (46), 10804−10811.
(37) Huang, Z.; Han, W.; Tang, H.; Ren, L.; Chander, D. S.; Qi, X.; Zhang, H. Photoelectrochemical-type sunlight photodetector based on MoS_2/graphene heterostructure. *2D Mater.* **2015**, *2* (3), 035011.
(38) Huang, W.; Xing, C.; Wang, Y.; Li, Z.; Wu, L.; Ma, D.; Dai, X.; Xiang, Y.; Li, J.; Fan, D.; Zhang, H. Facile fabrication and characterization of two-dimensional bismuth(iii) sulfide nanosheets for high-performance photodetector applications under ambient conditions. *Nanoscale* **2018**, *10* (5), 2404−2412.
(39) Li, Z.; Qiao, H.; Guo, Z.; Ren, X.; Huang, Z.; Qi, X.; Dhanabalan, S. C.; Ponraj, J. S.; Zhang, D.; Li, J.; Zhao, J.; Zhong, J.; Zhang, H. High-Performance Photo-Electrochemical Photodetector

DOI: 10.1021/acsanm.9b00527
ACS Appl. Nano Mater. 2019, 2, 4095−4103

Based on Liquid-Exfoliated Few-Layered InSe Nanosheets with Enhanced Stability. *Adv. Funct. Mater.* **2018**, *28* (16), 1705237.
(40) Ren, X.; Li, Z.; Huang, Z.; Sang, D.; Qiao, H.; Qi, X.; Li, J.; Zhong, J.; Zhang, H. Environmentally Robust Black Phosphorus Nanosheets in Solution: Application for Self-Powered Photodetector. *Adv. Funct. Mater.* **2017**, *27* (18), 1606834.
(41) Li, X.; Gao, C.; Duan, H.; Lu, B.; Pan, X.; Xie, E. Nanocrystalline TiO_2 film based photoelectrochemical cell as self-powered UV-photodetector. *Nano Energy* **2012**, *1* (4), 640−645.
(42) Guo, D.; Liu, H.; Li, P.; Wu, Z.; Wang, S.; Cui, C.; Li, C.; Tang, W. Zero-Power-Consumption Solar-Blind Photodetector Based on beta-Ga_2O_3/NSTO Heterojunction. *ACS Appl. Mater. Interfaces* **2017**, *9* (2), 1619−1628.
(43) Xie, Z.; Xing, C.; Huang, W.; Fan, T.; Li, Z.; Zhao, J.; Xiang, Y.; Guo, Z.; Li, J.; Yang, Z.; Dong, B.; Qu, J.; Fan, D.; Zhang, H. Ultrathin 2D Nonlayered Tellurium Nanosheets: Facile Liquid-Phase Exfoliation, Characterization, and Photoresponse with High Performance and Enhanced Stability. *Adv. Funct. Mater.* **2018**, *28* (16), 1705833.
(44) Zang, Z. Efficiency enhancement of ZnO/Cu_2O solar cells with well oriented and micrometer grain sized Cu_2O films. *Appl. Phys. Lett.* **2018**, *112* (4), 042106.
(45) Li, X.; Gao, C.; Duan, H.; Lu, B.; Wang, Y.; Chen, L.; Zhang, Z.; Pan, X.; Xie, E. High-performance photoelectrochemical-type self-powered UV photodetector using epitaxial $TiO_{(2)}/SnO_{(2)}$ branched heterojunction nanostructure. *Small* **2013**, *9* (11), 2005−11.
(46) Wei, J.; Guo, F.; Wang, X.; Xu, K.; Lei, M.; Liang, Y.; Zhao, Y.; Xu, D. SnO_2-in-Polymer Matrix for High-Efficiency Perovskite Solar Cells with Improved Reproducibility and Stability. *Adv. Mater.* **2018**, *30* (52), 1805153.
(47) Guo, D.; Wu, Z.; Li, P.; An, Y.; Liu, H.; Guo, X.; Yan, H.; Wang, G.; Sun, C.; Li, L.; Tang, W. Fabrication of β-Ga_2O_3 thin films and solar-blind photodetectors by laser MBE technology. *Opt. Mater. Express* **2014**, *4* (5), 1067.
(48) Dong, L.; Jia, R.; Xin, B.; Peng, B.; Zhang, Y. Effects of oxygen vacancies on the structural and optical properties of beta-Ga_2O_3. *Sci. Rep.* **2017**, *7*, 40160.
(49) Chen, K.; He, C.; Guo, D.; Wang, S.; Chen, Z.; Shen, J.; Li, P.; Tang, W. Low-voltage-worked photodetector based on Cu_2O/GaOOH shell-core heterojunction nanorod arrays. *J. Alloys Compd.* **2018**, *755*, 199−205.
(50) Guo, D. Y.; Wu, Z. P.; An, Y. H.; Guo, X. C.; Chu, X. L.; Sun, C. L.; Li, L. H.; Li, P. G.; Tang, W. H. Oxygen vacancy tuned Ohmic-Schottky conversion for enhanced performance in β-Ga_2O_3 solar-blind ultraviolet photodetectors. *Appl. Phys. Lett.* **2014**, *105* (2), 023507.
(51) Wei, H. M.; Gong, H. B.; Chen, L.; Zi, M.; Cao, B. Q. Photovoltaic Efficiency Enhancement of Cu_2O Solar Cells Achieved by Controlling Homojunction Orientation and Surface Microstructure. *J. Phys. Chem. C* **2012**, *116* (19), 10510−10515.
(52) Scanlon, D. O.; Morgan, B. J.; Watson, G. W. Modeling the polaronic nature of p-type defects in Cu_2O: the failure of GGA and GGA + U. *J. Chem. Phys.* **2009**, *131* (12), 124703.
(53) Xing, C.; Huang, W.; Xie, Z.; Zhao, J.; Ma, D.; Fan, T.; Liang, W.; Ge, Y.; Dong, B.; Li, J.; Zhang, H. Ultrasmall Bismuth Quantum Dots: Facile Liquid-Phase Exfoliation, Characterization, and Application in High-Performance UV-Vis Photodetector. *ACS Photonics* **2018**, *5* (2), 621−629.
(54) Yang, M.; Zhu, L.; Li, Y.; Cao, L.; Guo, Y. Asymmetric interface band alignments of Cu_2O/ZnO and ZnO/Cu_2O heterojunctions. *J. Alloys Compd.* **2013**, *578*, 143−147.
(55) Guo, D. Y.; Shi, H. Z.; Qian, Y. P.; Lv, M.; Li, P. G.; Su, Y. L.; Liu, Q.; Chen, K.; Wang, S. L.; Cui, C.; Li, C. R.; Tang, W. H. Fabrication of β-Ga_2O_3/ZnO heterojunction for solar-blind deep ultraviolet photodetection. *Semicond. Sci. Technol.* **2017**, *32* (3), 03LT01.
(56) Bai, Z.; Liu, J.; Liu, F.; Zhang, Y. Enhanced photoresponse performance of self-powered UV-visible photodetectors based on ZnO/Cu_2O/electrolyte heterojunctions via graphene incorporation. *J. Alloys Compd.* **2017**, *726*, 803−809.
(57) Yang, Y.; Zhang, H.; Lin, Z.-H.; Liu, Y.; Chen, J.; Lin, Z.; Zhou, Y. S.; Wong, C. P.; Wang, Z. L. A hybrid energy cell for self-powered water splitting. *Energy Environ. Sci.* **2013**, *6* (8), 2429.
(58) Yang, Y.; Zhang, H.; Liu, R.; Wen, X.; Hou, T.-C.; Wang, Z. L. Fully Enclosed Triboelectric Nanogenerators for Applications in Water and Harsh Environments. *Adv. Energy Mater.* **2013**, *3* (12), 1563−1568.
(59) Ouyang, B.; Zhang, K.; Yang, Y. Photocurrent Polarity Controlled by Light Wavelength in Self-Powered ZnO Nanowires/SnS Photodetector System. *IScience* **2018**, *1*, 16−23.
(60) Wen, J.; Xie, J.; Chen, X.; Li, X. A review on g-C_3N_4 -based photocatalysts. *Appl. Surf. Sci.* **2017**, *391*, 72−123.
(61) Jiang, T.; Xie, T.; Chen, L.; Fu, Z.; Wang, D. Carrier concentration-dependent electron transfer in $Cu_{(2)}O$/ZnO nanorod arrays and their photocatalytic performance. *Nanoscale* **2013**, *5* (7), 2938−44.
(62) Zhang, Z.; Wang, P. Highly stable copper oxide composite as an effective photocathode for water splitting via a facile electrochemical synthesis strategy. *J. Mater. Chem.* **2012**, *22* (6), 2456−2464.
(63) Higashiwaki, M.; Sasaki, K.; Kuramata, A.; Masui, T.; Yamakoshi, S. Gallium oxide (Ga_2O_3) metal-semiconductor field-effect transistors on single-crystal β-Ga_2O_3 (010) substrates. *Appl. Phys. Lett.* **2012**, *100* (1), 013504.
(64) Li, M.; Zhang, L.; Fan, X.; Zhou, Y.; Wu, M.; Shi, J. Highly selective CO_2 photoreduction to CO over g-C_3N_4/Bi_2WO_6 composites under visible light. *J. Mater. Chem. A* **2015**, *3* (9), 5189−5196.
(65) White, J. L.; Baruch, M. F.; Pander Iii, J. E.; Hu, Y.; Fortmeyer, I. C.; Park, J. E.; Zhang, T.; Liao, K.; Gu, J.; Yan, Y.; Shaw, T. W.; Abelev, E.; Bocarsly, A. B. Light-Driven Heterogeneous Reduction of Carbon Dioxide: Photocatalysts and Photoelectrodes. *Chem. Rev.* **2015**, *115* (23), 12888−935.
(66) Lin, S.; Wang, H. Y.; Zhang, X. N.; Wang, D.; Zu, D.; Song, J. N.; Liu, Z. L.; Huang, Y.; Huang, K.; Tao, N.; Li, Z. W.; Bai, X. P.; Li, B.; Lei, M.; Yu, Z. F.; Wu, Hui Direct Spray-Coating of Highly Robust and Transparent Ag Nanowires for Energy Saving Windows. *Nano Energy* **2019**, *62*, 111−116.

DOI: 10.1021/acsanm.9b00527
ACS Appl. Nano Mater. 2019, 2, 4095−4103